Astronomy & Astrophysics

Metal-THINGS: Association and optical characterization of supernova remnants with H I holes in NGC 6946

M. A. Lara-López[1], L. S. Pilyugin[2,3], J. Zaragoza-Cardiel[4,5], I. A. Zinchenko[6,3], O. López-Cruz[4],
S. P. O'Sullivan[7], M. E. De Rossi[8,9], S. Dib[10], L. E. Garduño[4], M. Rosado[11],
M. Sánchez-Cruces[11], and M. Valerdi[4]

[1] Departamento de Física de la Tierra y Astrofísica, Instituto de Física de Partículas y del Cosmos, IPARCOS, Universidad Complutense de Madrid (UCM), 28040 Madrid, Spain
e-mail: maritzal@ucm.es
[2] Institute of Theoretical Physics and Astronomy, Vilnius University, Sauletekio av. 3, 10257 Vilnius, Lithuania
[3] Main Astronomical Observatory, National Academy of Sciences of Ukraine, 27 Akademika Zabolotnoho St, 03680 Kiev, Ukraine
[4] Instituto Nacional de Astrofísica, Óptica y Electrónica (INAOE), Luis E. Erro 1, Tonantzintla, Puebla C.P. 72840 México, Mexico
[5] Consejo Nacional de Ciencia y Tecnología, Av. Insurgentes Sur 1582, 03940 Ciudad de México, Mexico
[6] Faculty of Physics, Ludwig-Maximilians-Universität, Scheinerstr. 1, 81679 Munich, Germany
[7] School of Physical Sciences and Centre for Astrophysics & Relativity, Dublin City University, Glasnevin D09 W6Y4, Ireland
[8] Universidad de Buenos Aires, Facultad de Ciencias Exactas y Naturales y Ciclo Básico Común, Buenos Aires, Argentina
[9] CONICET-Universidad de Buenos Aires, Instituto de Astronomía y Física del Espacio (IAFE), Buenos Aires, Argentina
[10] Max Planck Institute for Astronomy, Königstuhl 17, 69117 Heidelberg, Germany
[11] Instituto de Astronomía, Universidad Nacional Autonoma de México, Apartado Postal 70-264, CP 04510 México, CDMX, Mexico

ABSTRACT

Context. NGC 6946, also known as the "Fireworks Galaxy", is an unusual galaxy that hosts a total of 225 supernova remnant (SNR) candidates, including 147 optically identified with high [S II]/Hα line ratios. In addition, this galaxy shows prominent H I holes, which have been analyzed in previous studies. Indeed, the connection between SNRs and H I holes along with their physical implications in the surrounding gas are worthy of attention.
Aims. This paper explores the connection between the SNRs and the H I holes, including an analysis of their physical link to observational optical properties inside and around the rims of the holes, using new integral field unit (IFU) data from the Metal-THINGS survey.
Methods. We present an analysis combining previously identified H I holes, SNR candidates, and new integral field unit (IFU) data from Metal-THINGS of the spiral galaxy NGC 6946. We analyzed the distributions of the oxygen abundance, star formation rate surface density, extinction, ionization, and diffuse ionized gas, as well as the Baldwin-Phillips-Terlevich classification throughout the galaxy.
Results. By analyzing the optical properties of the 121 previously identify H I holes in NGC 6946 in detail, we find that the SNRs are concentrated at the rims of the H I holes. Furthermore, our IFU data show that the star formation rate and extinction are enhanced at the rims of the holes. To a lesser degree, the oxygen abundance and ionization parameter show hints of enhancement on the rims of the holes. Altogether, this provides evidence of induced star formation taking place at the rims of the holes, whose origin can be explained by the expansion of superbubbles created by multiple supernova explosions in large stellar clusters dozens of Myr ago.

Key words. galaxies: spiral – galaxies: abundances – galaxies: ISM

1. Introduction

NGC 6946, also known as the "Fireworks Galaxy" due to its high number of supernovae (SNe), is a nearly face-on galaxy, with a reported inclination angle between ~38° (Carignan et al. 1990; Boomsma et al. 2008), and ~32° (Bonnarel et al. 1988; de Blok et al. 2008).

Morphologically, NGC 6946 is a late-type SABcd galaxy (de Vaucouleurs et al. 1991) and hosts well-defined multiple spiral arms and three bars (e.g., Elmegreen et al. 1998; Schinnerer et al. 2006; Fathi et al. 2009; Romeo & Fathi 2015). Deep H I observations reveal the existence of regular and prominent spiral arms in the outer gaseous disk, well outside the optical disk (Boomsma et al. 2008; Bertin & Amorisco 2010). In addition, NGC 6946 is an isolated galaxy located in the nearby void (Sharina et al. 1997), although the presence of tidal encounters and minor mergers cannot be discarded (Boomsma et al. 2008).

Given its intriguing nature, NGC 6946 has been mapped at multiple wavelengths. For example, in the 21 cm atomic hydrogen emission line (e.g., Rogstad & Shostak 1972; Carignan et al. 1990; Boomsma 2007; de Blok et al. 2008), in Hα emission of the ionized hydrogen (e.g., Bonnarel et al. 1988; Blais-Ouellette et al. 2004; Daigle et al. 2006), in the molecular (CO) emission lines (e.g., Walsh et al. 2002; Leroy et al. 2009; Helfer et al. 2003; Romeo & Fathi 2015), with the *Hubble* Space Telescope (HST; Larsen 2004), and as part of large surveys, such as the Key Insights on Nearby Galaxies: a Far-Infrared Survey with *Herschel* (KINGFISH, Kennicutt et al. 2011), and the Spitzer Infrared Nearby Galaxies Survey (SINGS, Moustakas et al. 2010), among others.

In particular, NGC 6946 has been covered by the H I Nearby Galaxy Survey (THINGS) survey (Walter et al. 2008), which observed 34 large, nearby galaxies with the Very Large Array (VLA), obtaining high spatial and spectral resolution H I data. Therefore, the distribution of properties (surface mass density, velocity dispersion, and rotation velocity) of the atomic gas across the disk are available for this galaxy.

NGC 6946 is the most extreme known example of a galaxy with a high supernova rate. Ten supernova events have been observed since 1917 (Eldridge & Xiao 2019). A large number of supernova remnants (SNRs) and candidates have been identified in NGC 6946 in different ways (Matonick & Fesen 1997; Long et al. 2019, 2020). Recently, a large optical search of SNR was performed by Long et al. (2019) using the WIYN telescope (Kitt Peak National Observatory). A total of 225 SNR candidates were found by Long et al. (2020) using optical and IR data, including 147 SNRs identified as optical nebulae with high [S II/Hα] line ratios (Long et al. 2019).

One prominent feature detectable with H I observations is the existence of H I holes (Brinks & Bajaja 1986). Boomsma (2007) and Boomsma et al. (2008) studied the distribution and kinematics of the neutral gas in NGC 6946 at 21 cm with the Westerbork Synthesis Radio Telescope. They detected high-velocity H I gas and found 121 H I holes, most of which are located in the inner regions where the gas density and the star formation rate are higher. The sizes of the H I holes are up to 3 kpc diameter, while their ages are in the range of 1 to 6×10^7 yr[1]. Boomsma (2007) and Boomsma et al. (2008) conclude that stellar feedback (galactic fountain) is probably at the origin of most of the high-velocity gas and H I holes (see also Dib et al. 2021). That is to say, the most likely mechanism for producing H I holes is the expansion (and blow-up) of superbubbles created by multiple supernova explosions around large stellar clusters.

The number of holes in NGC 6946 and their sizes is still debatable. A later study by Bagetakos et al. (2011) found only 56 holes, although with an excellent agreement for the holes larger than 700 pc in comparison with Boomsma et al. (2008). Part of the disagreement can be attributed to the different resolution limit of each study. Moreover, both studies rely on a "by eye" identification of the H I holes, which is less quantifiable and prone to human error.

We observed NGC 6946 as part of the Metal-THINGS survey with integral field unit (IFU) spectroscopy. A mosaic was built with a collection of 12 pointings, which is, to the best of our knowledge, the largest collection of optical spectra of this galaxy to date. Our aim is to characterize the optical properties of this galaxy such as the oxygen abundance gradient and the SFR, as well as to characterize the SNRs and their possible effect on the aforementioned properties. Due to the starburst nature of this galaxy, we search as well for relations between the observed H I holes, SNRs, and star formation rate (SFR) enhancements. Throughout this paper, we use the most recent distance estimate using the tip of the red giant branch of 7.8 Mpc (Anand et al. 2018; Murphy et al. 2018).

This paper is organized as follows. The observations are described in Sect. 2. In Sect. 3, we determine the oxygen abundance, SFR surface density, ionization parameter, and color excess in NGC 6946. In Sect. 4, we present our results. Section 5 provides a discussion, and our conclusions are given in Sect. 6.

2. Observations

The Metal-THINGS survey is a large program focused on obtaining IFU spectroscopy of a unique sample of nearby galaxies with complementary imaging and spectroscopic mapping at multiple wavelengths. Our sample of galaxies is based on the THINGS survey (Walter et al. 2008), which observed 34 large, nearby radio galaxies with the Very Large Array (VLA), providing high spatial and spectral resolution H I data.

The Metal-THINGS survey is obtaining IFU data using the 2.7 m Harlan Schmidt telescope at McDonald Observatory, with the George Mitchel spectrograph (GMS, formerly known as VIRUS-P, Hill et al. 2008), which is a square array of 100×102 arcsec. The IFU consists of 246 fibers arranged in a fixed pattern, where each fiber has a 4.2 arcsec diameter. Every pointing is observed with three dither positions to ensure a 90% surface coverage (see Fig. 1 of Blanc et al. 2009). Due to the extended nature of our galaxies, sky exposures are taken offsource for sky subtraction purposes during the reduction process.

NGC 6946 was observed as part of the Metal-THINGS survey (Lara-López et al. 2021) through a red setup covering the wavelength range from 4400 to 6800 Å, with the low resolution grid (VP1), which provides a spectral resolution of ~5 Å FWHM. The wavelength range of the red setup allows us to measure the strongest emission lines: Hβ, [OIII]$\lambda\lambda$4959, 5007, [OI]λ6300, Hα, [NII]λ6584, and [SII]$\lambda\lambda$6716, 6731.

Our observing procedure consists on 15 min exposure per dither, followed by a sky exposure, and repetition of the process until 45 min are reached per dither, per pointing. A calibration star was observed every night using six dither positions to ensure a 99% flux coverage. Calibration lamps (Neon + Argon for the red setup) were observed at the beginning and end of every night to wavelength calibrate the spectra.

NGC 6946 was observed using GMS in June 2018, October 2018, October 2020, and June 2021. The average seeing during the observations was 1.5 arcsec. A total of 12 pointings were observed to form the mosaic shown in Fig. 1. The whole mosaic has a total of 8856 individual spectra. The astrometry was set by using all the fibers of individual pointings and their relative positions within each. First, we created a tridimensional cube associating each fiber to its relative spatial position in the pixel (x,y) plane and convolving by a Gaussian with a FWHM of 4″.2 (the diameter of the fiber) at each wavelength. Next, from the spectral-dimension collapsed image we identified several stars and used the same star positions from 2MASS images to set an absolute astrometry for each pointing. We repeated this process for each pointing to create the mosaic of Fig. 1. Even though our initial pointings were aligned next to each other, since the observing runs spread over several years, we attribute the observed shifts to variations in the instrumentation setups.

The galaxy NGC 6946 is at a distance of about 7.8 Mpc (Anand et al. 2018; Murphy et al. 2018) which gives a scale of 37.8 pc/″, so that each 4″.2 fiber in the IFU corresponds to ~158.8 pc. The optical radius of NGC 6946 (R_{25} = 344.45 arcsec) is taken from the NASA/IPAC Extragalactic Database (NED)[2]. With the adopted distance, this gives an optical radius of R_{25} = 13.02 kpc.

The basic data reduction including bias subtraction, flat frame correction, and wavelength calibration, was performed

---

[1] Boomsma (2007) and Boomsma et al. (2008) adopt a distance of 6 Mpc to NGC 6946, while recent distance estimates using the tip of the red giant branch result in a value of around 7.8 Mpc (Anand et al. 2018; Murphy et al. 2018). This implies that the sizes and ages of the H I holes can be underestimated by around thirty per cent.

[2] The NASA/IPAC Extragalactic Database (NED) is operated by the Jet Populsion Laboratory, California Institute of Technology, under contract with the National Aeronautics and Space Administration. http://ned.ipac.caltech.edu/
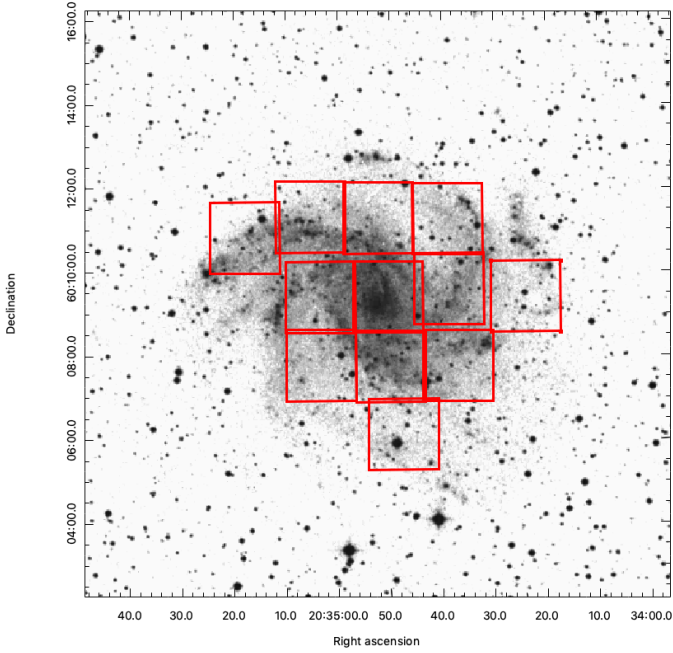
Fig. 1. Observed 12 pointings superimposed on the NGC 6946 image. Each individual box corresponds to the field of view of the George Mitchel spectrograph (GMS, formerly known as VIRUS-P).

Fig. 2. Identification of DIG based on the extinction corrected Hα flux and C_{HII}. The dashed and dotted horizontal lines show the median [S II]/Hα for the 100 brightest and 100 dimmest fibers, respectively. The vertical solid line shows the value of $\log(f_0)$. The red solid line shows the fit of Eq. (2) to our data.

using P3D[3]. The sky subtraction and the combination of dithers was performed using our own routines in Python. Flux calibration was performed following Cairós et al. (2012) using six dither positions, ensuring 99% coverage. Next, we used IRAF (Tody et al. 1986) to create a flux calibration function using the standard and sensfunc packages.

The stellar continuum of all flux-calibrated spectra was fitted using STARLIGHT (Cid et al. 2005; Mateus et al. 2006; Asari et al. 2007). Briefly, we used 45 simple stellar population (SSP) models from the evolutionary synthesis models of Bruzual & Charlot (2003) with ages from 1 Myr up to 13 Gyr and metallicities $Z = 0.005, 0.02$ and 0.05. The reddening law of Cardelli et al. (1989) was adopted, assuming $R_v = 3.1$. Next, the fitted continuum was subtracted from the spectra, and the emission lines were measured using Gaussian line-profile fittings. It should be noted that only those fiber spectra where all the used lines were measured with a signal-to-noise ratio $(S/N) > 3$ were considered. For a more detailed description, see Zinchenko et al. (2016).

In this paper, we use the individual spectra of the fibers, which are independent of each other. This is in contrast to the spaxel spectra in surveys such as the Mapping Nearby Galaxies at Apache Point Observatory survey (MaNGA), where the point spread function (PSF) is estimated to have a FWHM of 2.5″ (Bundy et al. 2015; Belfiore et al. 2017). Our IFU spectroscopy and derived astrometry provide the possibility to construct the maps of the oxygen abundance (and other characteristics) in the disk and to investigate the global and local properties of the abundance distribution (Lara-López et al. 2021).

3. Physical properties of NGC 6946

The geometrical parameters of the galaxy, namely, the location of the center of the galaxy, the position angle of the major

---
[3] https://p3d.sourceforge.io
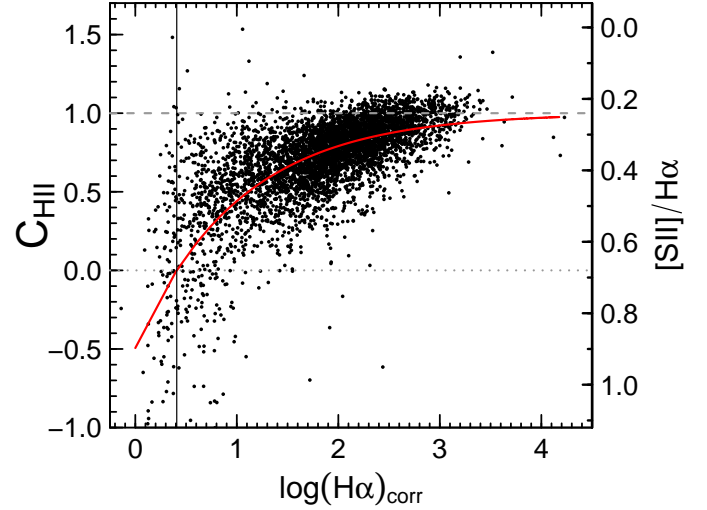
---

axis, and the inclination angle, are needed to determine the galactocentric distances of the fibers.

In this paper, we use the position of the center obtained by Trachternach et al. (2008; RA = 20^h 34^m $52\overset{s}{.}2$ and Dec = $+60°$ $09'$ $14\overset{''}{.}4$), and the position angle of the major kinematic axis (PA = $242\overset{\circ}{.}7$) as well as the inclination angle ($i = 32\overset{\circ}{.}6$) obtained by de Blok et al. (2008).

The stellar mass estimates for this galaxy show an appreciable spread. At a distance of 5.9 Mpc, using data from the *Spitzer* Infrared Nearby Galaxies Survey, de Blok et al. (2008) found the mass value to be within the range $\log(M_\star/M_\odot) \sim 10.58 - 10.77$. On the other hand, Jarrett et al. (2019) found a value of $\log(M_\star/M_\odot) = 10.26$ using the mid-infrared luminosity from the Wide-field Infrared Survey Explorer (WISE). NGC 6946 does not show a classical bulge but has a tiny pseudobulge and there is no evidence that this galaxy hosts an AGN (Kormendy et al. 2010).

3.1. Diffuse ionized gas

The diffuse ionized gas (DIG), also known as the warm ionized medium (WIM), is a warm ($\sim 10^4$ K), low density ($\sim 10^{-1}$ cm^{-3}) gas phase found in the interstellar medium of galaxies (Reynolds 1984). DIG is an important component in star-forming galaxies, and its contribution to emission line fluxes can affect and impact the interpretation of measured metallicities, ionization, and BPT diagrams (Baldwin et al. 1981) in galaxies. Several approaches have been proposed for the identification of DIG using IFU spectroscopy (e.g., Poetrodjojo et al. 2019; Kaplan et al. 2016).

To determine the fraction of flux originating from H II regions and from the DIG (named C_{HII}), we used the method first proposed by Blanc et al. (2009), and further developed by Kaplan et al. (2016). This method relies on the assumption that the brightest fiber fluxes are dominated by H II emission, while the dimmest ones are dominated by DIG emission. Following Kaplan et al. (2016), we first estimated the characteristic value of [S II]/Hα in the brightest fibers for H II regions ([S II]/Hα)$_{HII}$, and in the dimmest ones for DIG ([S II]/Hα)$_{DIG}$. Only fibers with a $S/N > 3$ in Hα, Hβ, and [S II] are included in this analysis.

In each fiber, we make an initial guess for $C_{H\,II}$:

$$C_{H\,II} = \frac{[S\,II]/H\alpha - ([S\,II]/H\alpha)_{DIG}}{([S\,II]/H\alpha)_{H\,II} - ([H\,II]/H\alpha)_{DIG}}. \qquad (1)$$

Next, by using the initial estimate of $C_{H\,II}$ and the extinction corrected $f(H\alpha)$, we fit the data for f_0 and β in the following expression:

$$C_{H\,II} = 1 - \left(\frac{f_0}{f(H\alpha)}\right)^{\beta}, \qquad (2)$$

obtaining $f_0 = 2.56 \pm 0.12$, and $\beta = 0.427 \pm 0.007$, shown by the red solid line in Fig. 2. A final value for $C_{H\,II}$ is provided by Eq. (2) using the best-fit coefficients.

While all regions where $H\alpha_{corr} < f_0$ are 100% DIG dominated, a somewhat arbitrary threshold in $C_{H\,II}$ is needed to select the DIG, which is based on the dimmest fluxes in the observed sample. In this paper, we define fibers with $C_{H\,II} < 0.4$ as dominated by DIG, which are flagged in the rest of our analysis. In Fig. 3, we show the fibers identified as DIG in small black circles, which corresponds to 9.2% of the analyzed sample.
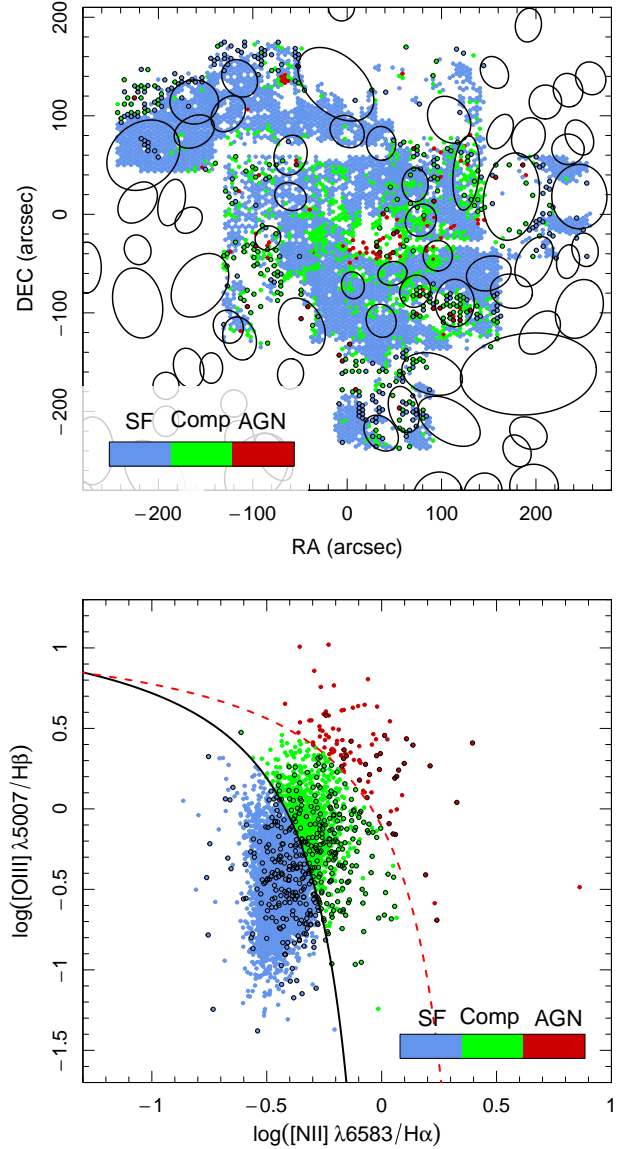
3.2. BPT classification

The measured emission line fluxes of each fiber spectra are corrected for the interstellar reddening using the reddening law from Cardelli et al. (1989) with $R_V = 3.1$. The value of the interstellar reddening is estimated through the comparison between the measured and the theoretical $H\alpha/H\beta$ ratio (that is, using the standard value of $H\alpha/H\beta = 2.86$). When the measured value of $H\alpha/H\beta$ is lower than 2.86, the reddening is assumed to be zero. We adopted $C_{H\beta} = 0.47A_V$ (Lee et al. 2005).

We classify every spectra using its location in the [N II]$\lambda6584$/Hα versus [O III]$\lambda5007$/Hβ line ratio diagram suggested by Baldwin et al. (1981, BPT diagram), The NGC 6946 map and BPT classification is shown in Fig. 3. As in our previous studies (Zinchenko et al. 2019; Pilyugin et al. 2020a,b, 2021a,b; Lara-López et al. 2013), the spectra located to the left (below) the demarcation line from Kauffmann et al. (2003), shown as blue symbols in the two panels of Fig. 3, are referred to as the SF-like or H II region-like spectra. Those located to the right (above) the demarcation line from Kewley et al. (2001), shown as red symbols in Fig. 3, are referred to as the AGN-like spectra. The spectra located between those demarcation lines are Composite, or intermediate spectra, shown as green symbols in Fig. 3. In both panels of Fig. 3, the black circles denote regions dominated by DIG.

3.3. Oxygen abundance and ionization parameter

Here, we estimate the oxygen abundance for the fibers classified as H II region-like by the BPT. The oxygen lines [O II]$\lambda3726$ and $\lambda3729$ are beyond the spectral range of our red GMS spectra. Hence, the calibrations which involve those lines cannot be used for abundance determinations with our current data. From the plethora of available methods, we use the three-dimensional (3D) S calibration O/H = $f(N2, S2, R3/S2)$ from Pilyugin & Grebel (2016). The advantage of 3D calibrations for the abundance determinations in comparison to 1D calibrations is discussed in Pilyugin et al. (2018). The S calibration consists of an upper (high metallicity) and lower (low metallicity) branches. The transition from the upper to lower branch occurs

Fig. 3. BPT classification in NGC 6946. Top panel: Map of the BPT classification, color-coded as indicated in the label. Bottom panel: BPT diagram for the individual fibers with SF-like spectra (blue symbols), Composite (green symbols), and AGN-like (red symbols). The black solid and red dashed curves are the demarcation lines between SF and AGN regions defined by Kauffmann et al. (2003) and Kewley et al. (2001), respectively. The ellipses in the top panel indicate the H I holes (see Sect. 4.2), while the small black circles denote regions dominated by DIG.

at $\log N_2 \approx -0.6$. The corresponding calibration relation for the upper branch ($\log N_2 > -0.6$) is:

$$\begin{aligned}(O/H)^*_{S,U} &= 8.424 + 0.030 \log(R_3/S_2) + 0.751 \log N_2 \\ &+ (-0.349 + 0.182 \log(R_3/S_2) + 0.508 \log N_2), \qquad (3) \\ &\times \log S_2,\end{aligned}$$

where we use the notation $(O/H)^*_{S,U} = 12 + \log(O/H)_{S,U}$ for a compact way. The calibration for the lower branch ($\log N_2 < -0.6$) is:

$$\begin{aligned}(O/H)^*_{S,L} &= 8.072 + 0.789 \log(R_3/S_2) + 0.726 \log N_2 \\ &+ (1.069 - 0.170 \log(R_3/S_2) + 0.022 \log N_2), \qquad (4) \\ &\times \log S_2\end{aligned}$$

where $(O/H)^*_{S,L} = 12 + \log(O/H)_{S,L}$.

Since the [O III]$\lambda 5007$ and $\lambda 4959$ lines originate from transitions from the same energy level, their flux ratio is defined only by the transition probability ratio, which is close to 3 (Storey & Zeippen 2000). The line measurement of the stronger line [O III]$\lambda 5007$ is usually more precise than that for the weaker line [O III]$\lambda 4959$. Therefore, we estimated the value of R_3 as $R_3 = 1.33$ [O III]$\lambda 5007$/Hβ. Similarly, we estimated the value of N_2 as $N_2 = 1.33$ [N II]$\lambda 6584$/Hβ. The metallicity gradient and map, will be further analyzed in Sects. 4.1 and 4.3, respectively.

The ionization parameter is defined as $U = Q_{\text{ion}}/4\pi R_{\text{in}}^2 nc$, where Q_{ion} is the number of hydrogen ionizing photons emitted per second by the ionizing source, R_{in} is the distance from the ionization source to the inner surface of the ionized gas cloud, n is the particle density, and c is the speed of light. We estimate the ionization parameter following the prescription of Dors et al. (2017):

$$\log(U)_D = c \times S2 + d, \tag{5}$$

where $S2 = \log([\text{S II}]\lambda\lambda\, 6717{,}31\, /\, \text{H}\alpha)$, $c = -0.26 \times (Z/Z_\odot) - 1.54$, and $d = -3.69 \times (Z/Z_\odot)^2 + 5.11 \times (Z/Z_\odot) - 5.26$. For the oxygen abundance of the Sun, we use $Z_\odot = 8.69$ (Amarsi et al. 2018). Since the oxygen abundance is needed for the ionization parameter estimation, the final sample is the same (4154 fibers). The resulting ionization will be analyzed in Sect. 4.3.

3.4. Star formation rates and color excess

In this section, we estimate the SFRs and color excess that will be further analyzed in detail in Sect. 4.3.

The resolved SFR is estimated using the Hα prescription of Kennicutt et al. (2009; see also the review of Calzetti 2013), which uses an Kroupa (2001) initial mass function (IMF).

$$\text{SFR}[\text{Myr}^{-1}] = 5.5 \times 10^{-42} L_{\text{corr}}(\text{H}\alpha_{\text{corr}})\, \text{ergs}^{-1}, \tag{6}$$

where Hα_{corr} is the Hα flux corrected by extinction. The estimated SFRs are then converted to SFR surface densities ($\sum_{\text{SFR}}$) by dividing them by the area on the sky of the 4.2″ diameter fiber. The SFR was measured only in fibers whose spectra are classified as SF or Composite in the BPT diagram, and have a $S/N > 3$ in Hα and Hβ. The final SFR sample used is formed by 4972 fiber spectra.

Finally, we estimated the color excess $E(B - V)$ as an indicator of the dust content, (e.g., Calzetti et al. 1996). For its estimation, different ratios from Hydrogen recombination lines can be used. For our sample, we are using Hα and Hβ, and the prescription of Calzetti et al. (1994) in the following:

$$E(B - V)_{\text{gas}} = \frac{\log(R_{\text{obs}}/R_{\text{int}})}{0.4\,[\,k(\lambda_{\text{H}\alpha}) - k(\lambda_{\text{H}\beta})\,]}, \tag{7}$$

where the observed radio R_{obs} is the Balmer decrement (Hα/Hβ), and the intrinsic ratio R_{int} is 2.86, taking a case B recombination (Osterbrock 1989). Finally, $k(\lambda)$ corresponds to the dust extinction curve, in this case, we use Calzetti et al. (2000), which is based on a set of starburst galaxies, appropriate for this analysis. The color excess was estimated using the same exclusion criteria as for the SFR.

4. Results

4.1. Oxygen abundance gradient and supernova remnants

NGC 6946 is the most extreme example of a galaxy with a high supernova rate, with ten supernova events since 1917
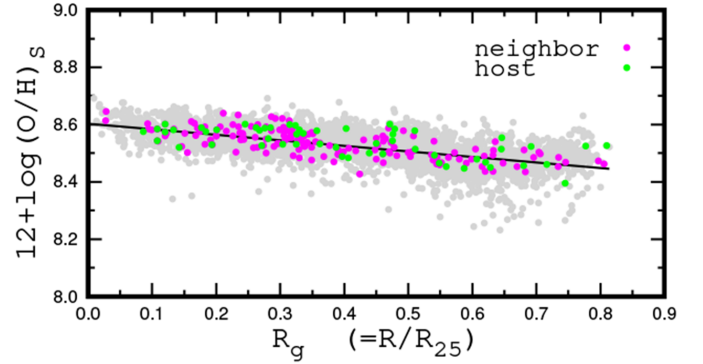
Fig. 4. Radial distribution of the oxygen abundance. The grey points denote the oxygen abundance of the individual fibers. The solid line is the best fit to the data. The green points mark the fibers hosting SNRs, while the magenta points correspond to the neighboring fibers to the SNRs positions.

(Eldridge & Xiao 2019). A large number of SNR and candidates have been identified in NGC 6946 in different ways (e.g., Matonick & Fesen 1997; Lacey et al. 1997; Lacey & Duric 2001; Bruursema et al. 2014; Long et al. 2019, 2020), amounting to a total of 225 SNR candidates. In this section, we explore whether the oxygen abundance is affected in the immediate environment of the SNR.

To this aim, first we estimate the oxygen abundance gradient for the whole galaxy. The gas metallicity estimated through strong emission lines give important clues on the physical properties of the ISM and formation and growth of galaxies. Negative gas metallicity gradients are widely found in late-type galaxies in the local universe (e.g., Zaritsky et al. 1994; Pilyugin et al. 2004, 2014; Moustakas et al. 2010; Belfiore et al. 2017; Lara-López & Galán-de 2022). Such negative gradients are consistent with an inside-out growth scenario of the disks (e.g., White & Frenk 1991; Mo et al. 1998).

The gradient O/H = $f(R)$ is approximated by a linear relation of the type 12+log(O/H) = 12+log(O/H)$_0$ + grad $\times R_g$, where 12+log(O/H)$_0$ is the oxygen abundance at the center of the galaxy, grad is the gradient in units of dex/R_{25}, and R_g is the radius normalized to the optical radius of the galaxy R_{25}. We find the following expression for the SF fibers in the disk of NGC 6946:

$$12 + \log(\text{O/H}) = 8.603(\pm 0.002) - 0.1938(\pm 0.0037) \times R_g. \tag{8}$$

The mean value of the scatter around this relation is 0.0429 dex. The solid line of Fig. 4 shows the obtained relation. In comparison with other galaxies and considering NGC 6946 has a stellar mass of $10^{10.26}\,M_\odot$ (Jarrett et al. 2019), our measured gradient is in agreement with galaxies of similar stellar masses from Kreckel et al. (2019) and Zinchenko et al. (2021). A more detailed analysis on the metallicity gradients of Metal-THINGS galaxies will be presented in Lara-López et al. (in prep.).

Next, to explore the effect of the SNRs on their environment, we need to obtain the fibers overlapping (hosting) with SNRs from the condition that the separation between the center of the fiber and the SNR is less than the fiber radius ($r_{\text{fiber}} = 2.1$ arcsec); otherwise a fraction of the SNR would be beyond the field of the host fiber. Moreover, the uncertainty in the coordinates of the fibers is around one arcsec and could be larger for some pointings. This can result in the incorrect identification of some fibers hosting SNRs. To take this possibility into account, we also obtain a "neighboring" fiber(s) for each SNR from the
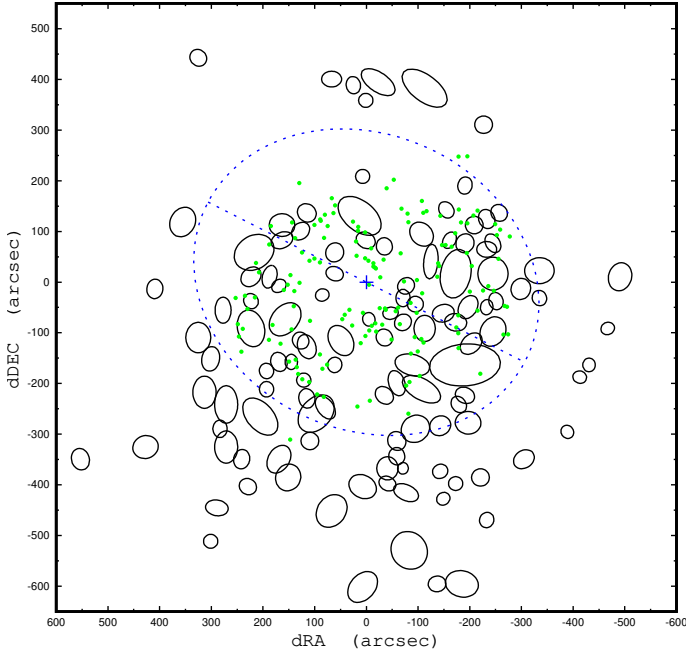
Fig. 5. H I holes and supernova remnants in the galaxy NGC 6946. The sizes and orientations of H I holes are indicated by the black solid ellipses. The green points show the positions of the SNRs. The dashed blue ellipse denotes the optical radius of the galaxy, the plus sign marks the position of the center, and the dashed line denotes the position of the major axis.
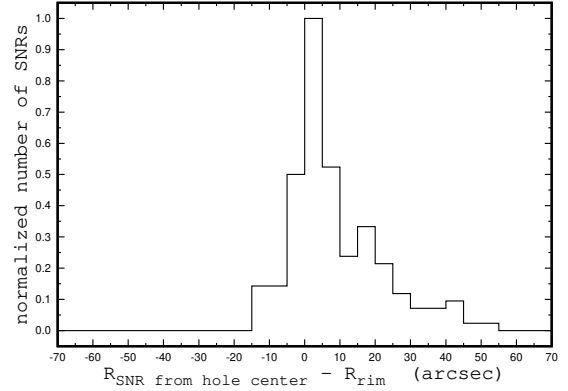

Fig. 6. Histogram of the difference between the SNR distance to the closest H I hole center, and the H I hole rim distance to the hole center (in the line from the center to the SNR).

condition that the separation between the SNR and the center of the fiber is larger than r_{fiber} and lower than $r_{fiber} + 2$ arcsec. Thus, the SNR could make a contribution to the radiation in the host or neighboring fiber, or even both, if the SNR is located in between them.

Most of host fibers are located in the SF region of the BPT diagram. Hence, this provides evidence that the contribution of the SNR radiation to the fiber spectra is not significant. Since the majority of the host and neighboring fibers show H II like spectra, their oxygen abundances are determined through the *S* calibration as indicated in Sect. 3.3. The fibers hosting SNRs are indicated as green points in Fig. 4, while the magenta points denote the neighboring fibers. It can be appreciated that there is no systematic difference or shift between the oxygen abundance of the fibers hosting SNRs and the rest of the fibers.

Altogether, we find no appreciable difference in the properties of the gas (BPT type and abundance) in fibers hosting SNRs in comparison with the rest. This suggests that the radiation of SNRs makes a small contribution to the radiation in the fiber field.

4.2. On the relation between SNRs and H I holes

As indicated in the introduction, Boomsma (2007) and Boomsma et al. (2008) identified and characterized 121 H I holes, most of which are located in the inner regions where the gas density and the star formation rate are higher. The origin of these H I holes is analyzed in detail in Boomsma et al. (2008). In general, they found that smaller holes up to 1 kpc in size, are more likely to be caused by SN feedback. However, it remains puzzling that many H I holes in NGC 6946 are observed without progenitor remnants. Also, they observed high velocity H I gas, that is likely produced by the blown-out (into the halo) of

the superbubbles that produce the holes in the disk, in agreement with the galactic fountain model (Collins et al. 2002). In addition, larger holes could be a blend of a number of smaller ones, or even be caused by the combination of thermal and gravitational instability (Dib & Burkert 2005). Since the likely origin for most of these H I holes is related to superbubbles created by multiple supernovae explosions, in this section, we explore such a connection.

In Fig. 5, we show the distribution of H I holes and recent SNRs across the image of NGC 6946. The sizes and orientations of the H I holes are indicated by the black solid ellipses, while the green points show the positions of the SNRs. For this study, we use the sample of SNR candidates from Long et al. (2019), who identified 147 candidates, using narrowband images, based on their elevated [S II]$\lambda\lambda$6716+6731/Hα ratios (Mathewson & Clarke 1973).

An inspection of Fig. 5 suggests that recent SNRs tend to avoid the H I holes and, in fact, SNRs are mostly distributed in the rims of the H I holes. To quantify this effect, we estimated two distances: (a) the distance from the SNR to the closest H I hole center (R_{SNR}) and (b) the distance from the H I hole center to the rim of the hole in the direction of the SNR (R_{rim}). A histogram of the differences between distances (a) and (b) is shown in Fig. 6. Every SNR is counted only once, and with respect to the closest hole center. The peak around zero in this histogram indicates an excess of SNRs coincident with the rims of the H I holes. The skewness of the histogram towards positive differences highlights that there are only a few SNRs lying within the H I holes. Since the inclination angle of NGC 6946 is ~32.6° (Bonnarel et al. 1988; de Blok et al. 2008), projection effects could in principle alter the distribution of the histogram in Fig. 6. However, we estimate a maximum ~15 % correction in the obtained distances.

On the other hand, the H I holes are not related to the BPT classification of the individual fibers. Instead, different BPT classifications take place within and outside the H I holes, as shown in Fig. 3. Also, the same figure shows that the DIG does not tend to dominate regions inside the holes, with only ~10% of DIG residing within the holes.

4.3. The physical properties of H I holes and rims

The excess of SNRs associated with the H I holes rims offers evidence that the induced star formation takes place in the shells of some superbubbles created by multiple supernova explosions
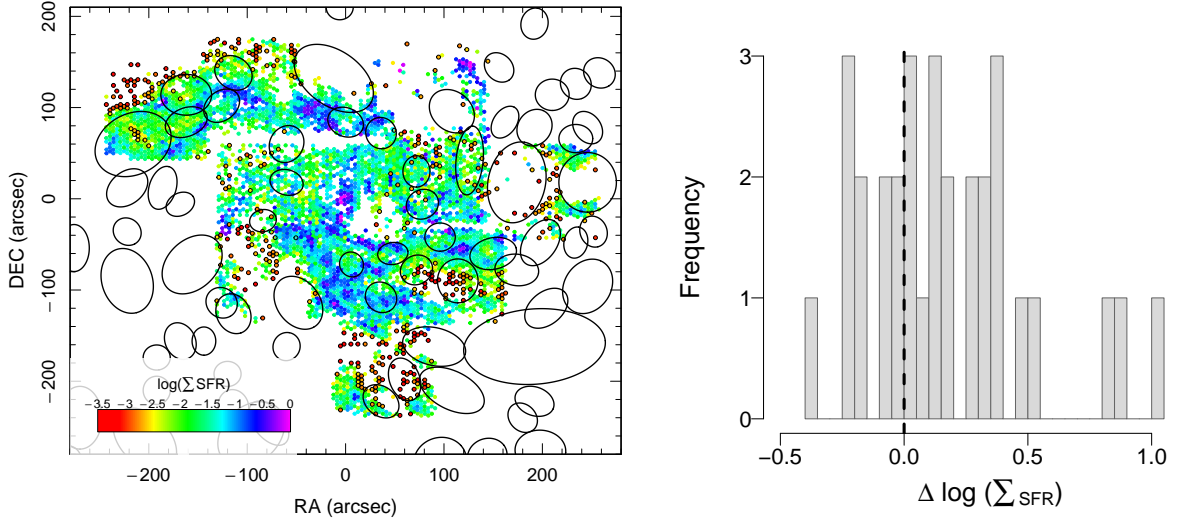
Fig. 7. Star formation rate surface densities in NGC 6946. Left: H I holes (black solid ellipses) superimposed on the log($\sum_{SFR}$) map of NGC 6946. The small black circles indicate DIG dominated fibers. Right: Histogram of the differences $\Delta \log(\sum_{SFR}) = \log(\sum \widehat{SFR_{rim}}) - \log(\sum \widehat{SFR_{hole}})$, see text for details.

at their centres dozens of Myr ago. Figure 7 (left) shows the log($\sum_{SFR}$) map of NGC 6946 together with the H I holes superimposed. A close examination of this map suggests that the $\sum_{SFR}$ tend to increase towards the H I hole rims. To examine this effect we estimated two $\sum_{SFR}$ for the whole sample, (*i*) the median star formation surface density inside each hole $\sum \widehat{SFR_{hole}}$, which corresponds to the median values of the fibers from the center of the hole to up to 79% of the distance from the center to the edge of the ellipse that define each hole and (*ii*) the median for the holes rims $\sum \widehat{SFR_{rim}}$, which corresponds to the median value of the fibers within 80% to 130% of the distance from the center to the edge of the ellipse of each hole. The same selection of fibers inside the holes and in the rims is followed in the next sections, although the number of holes analyzed will slightly change due to the different number of fibers used. The use of different distances to define center and rim fibers do not change our results drastically.

The difference $\Delta \log(\sum_{SFR}) = \log(\sum \widehat{SFR_{rim}}) - \log(\sum \widehat{SFR_{hole}})$ is estimated only when more than eight fibers are available in both, inside and in the rims of each hole, giving us a total of 31 holes. The histogram of these differences is shown in Fig. 7 (right), where it is clear that the histogram is skewed towards larger differences. From our sample, ~67.7% of the holes show an enhanced $\sum_{SFR}$ in their rims. To further quantify the degree of difference between rims and holes, we estimated a paired t-test, and obtained a t = 2.85, and a *p*-value = 0.007, meaning that there is a 0.7% probability that our result happened by chance; hence, we can reject the null hypothesis. When we discard the fibers previously identified as DIG (small circles in Fig. 7) and perform the same exercise, our sample is reduced to 28 holes, while the SFR enhancement in the rims holds, with ~64% of the difference showing a $\Delta \log(\sum_{SFR}) > 0$.

Following the same methodology, we analyzed the color excess $E(B - V)$ as an indicator of dust extinction. We use the same sample used for the SFRs. The obtained $E(B - V)$ map is shown in Fig. 8 (left). We analyze the color excess inside the holes and in the rims for 31 holes. The histogram of the difference $\Delta E(B - V) = E(\widehat{B - V})_{rim} - E(\widehat{B - V})_{hole}$, is shown in Fig. 8 (right). The color excess histogram indicates a skewness towards higher values in the rims, with a total of ~61% of holes showing a higher color excess in their rims. We run a paired t-test, and

obtained a t = 2.17, and a *p*-value = 0.03, hence, our data suggest higher dust extinction on the hole's rims. If fibers identified as DIG are not considered, the percentage of $\Delta E(B - V) > 0$ remains at ~61%.

We did the same exercise for the oxygen abundance and ionization parameter. Since the oxygen abundance and ionization parameter have the most restrictive criteria, we were able to analyze only 29 holes. The map of 12+log(O/H) is shown in Fig. 9 (left), while its respective histogram of the difference Δ 12+log(O/H) = $12 + \widehat{\log(O/H)}_{rim} - 12 + \widehat{\log(O/H)}_{hole}$ in Fig. 9 (right). The histogram indicates a minor shift towards higher abundances, with ~58.6% of our data showing higher differences. The paired t-test indicate a *t* = 1.45, and a *p*-value = 0.16. Hence, the difference in oxygen abundance between holes and rims is minor. Our results do not change when we exclude DIG dominated fibers (green circles in Fig. 9).

Similarly, the ionization parameter is displayed in Fig. 10 (left), while its respective histogram of the difference $\Delta \log(U) = \widehat{\log(U)}_{rim} - \widehat{\log(U)}_{hole}$, is shown in Fig. 10 (right). The t-test indicate that we cannot reject the null hypothesis with $t = 0.72$, *p*-value = 0.48. Hence, we conclude that there is not a statistically significant difference in the ionization parameter between holes and rims. However, the histogram is skewed towards higher ionization parameter differences, with ~66% of the holes showing positive differences.

From our statistical analysis, both the t-test and the skewness in the histogram show that the SFR has the strongest difference between the holes and the rims. To a lesser degree, $E(B - V)$ shows as well a clear enhancement on the rims. On the other hand, the t-tests do not show a statistical significant difference between the chemical abundance and the ionization. However, both show a skewness in their histogram towards positive differences, which is especially higher for the ionization, with a ~66% of the holes showing an enhancement on the rims.

5. Discussion

In this section, we discuss the physical implications of the over-abundance of SNRs in the rims of the H I holes. As indicated in Sect. 4.3, a remarkable feature in NGC 6946 is the existence
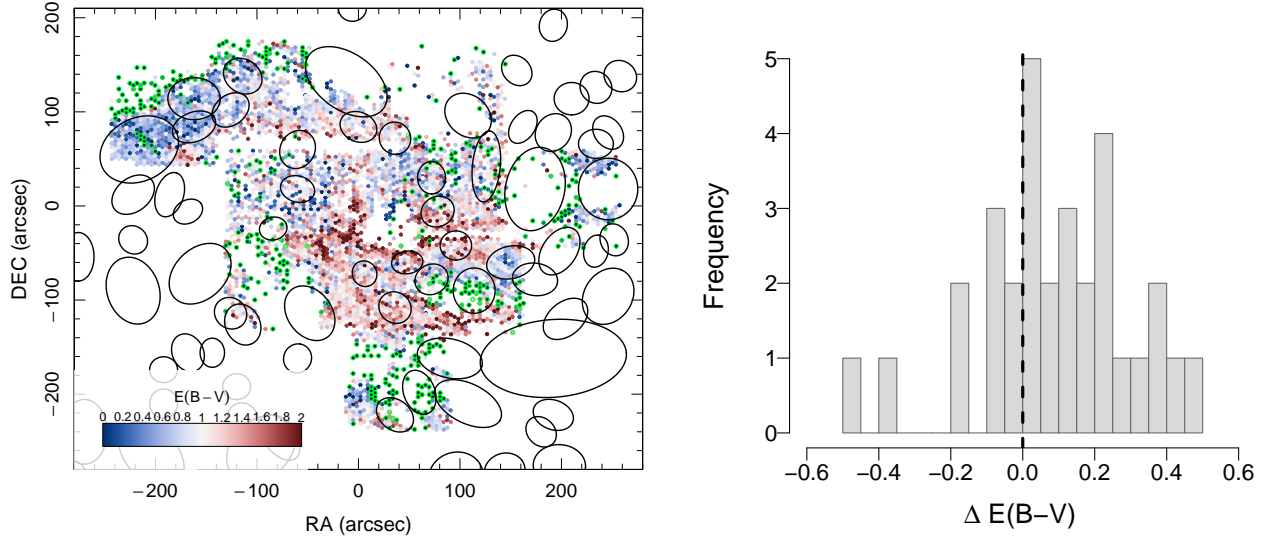
Fig. 8. $E(B-V)$ distribution in NGC 6946. Left: H I holes (black solid ellipses) superimposed on the E(B-V) map of NGC 6946. The small green circles indicate DIG dominated fibers. Right: Histogram of the differences $\Delta E(B-V) = E(\widehat{B-V})_{rim} - E(\widehat{B-V})_{hole}$, see text for details.
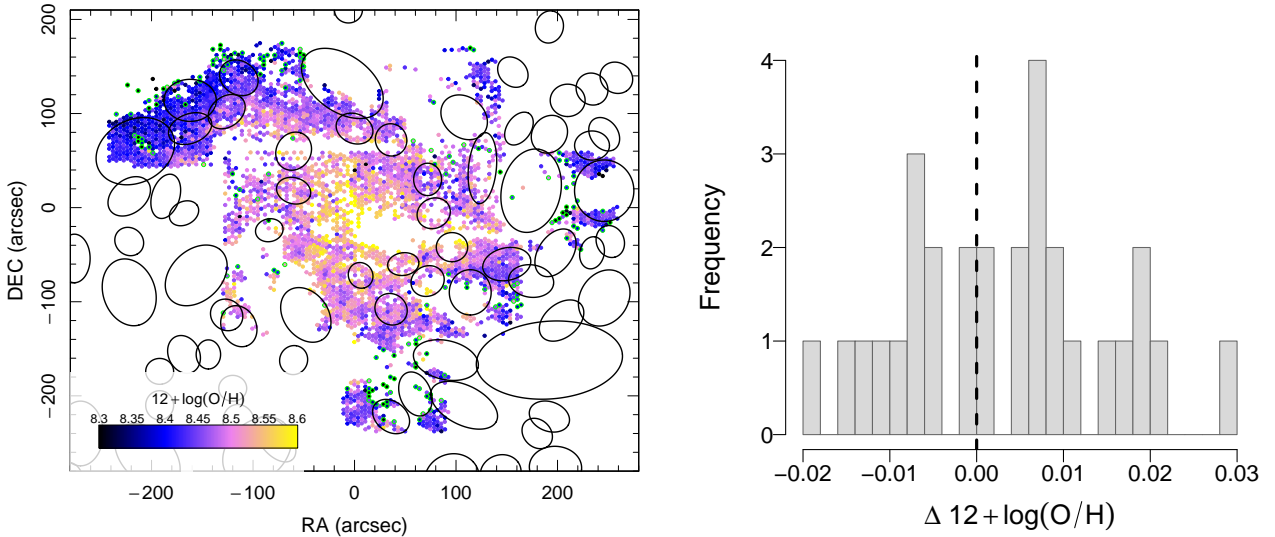
Fig. 9. Oxygen abundance in NGC 6946. Left: H I holes (black solid ellipses) superimposed on the 12+log(O/H) map of NGC 6946. The small green circles indicate DIG dominated fibers. Right: Histogram of the differences $\Delta 12 + \log(\mathrm{O/H}) = 12 + \widehat{\log(\mathrm{O/H})}_{rim} - 12 + \widehat{\log(\mathrm{O/H})}_{hole}$, see text for details.

and classification of 121 H I holes (Boomsma et al. 2008). Our data indicate an overabundance of SNRs located around the rims of the H I holes (Fig. 6). The H I holes in NGC 6946 were analyzed in detail by Boomsma et al. (2008), and they concluded that the creation of some of the holes can be attributed to the expansion of superbubbles generated by multiple SN explosions (e.g., Dib et al. 2006; Bagetakos et al. 2011; Dib et al. 2021). In addition, they found that stellar feedback in the form of a galactic fountain is probably the origin of some of the H I holes. This is in agreement with the lack of bright emission at multiple wavelengths inside the holes, suggesting that the H I holes are already devoid of gas, which could also explain the lack of SNRs located inside the holes.

As shown in Sect. 4.3, we observe a clear enhancement in SFR and dust extinction on the hole's rims, and to a minor degree, the gas metallicity and ionization parameter. The star formation is a complex process that is affected by internal and

external mechanisms, as well as the aforementioned properties to different degrees. For instance, since the existence of dust in galaxies affects the star-formation activity, it is not surprising that the observed enhancement in SFR is accompanied by a higher dust extinction in the hole's rims. Indeed, it has been shown that dust grains increase the molecular formation rate by two orders of magnitude compared to the case without dust (Hollenbach & McKee 1979), drastically enhancing the star formation activity (e.g., Asano et al. 2013). Hence, it makes sense that bursts of star formation are associated with areas of high dust extinction.

Furthermore, the excess dust we observe in the hole's rims is likely produced by the SNRs. It is known that SNe are very efficient dust producers (mainly core-collapse Type II-P, i.e., there is a plateau in their light curve), as well as dust destroyers (i.e., the pressure of the ISM gas that is shocked by the expanding SNe blast wave generates a reverse shock that propagate through
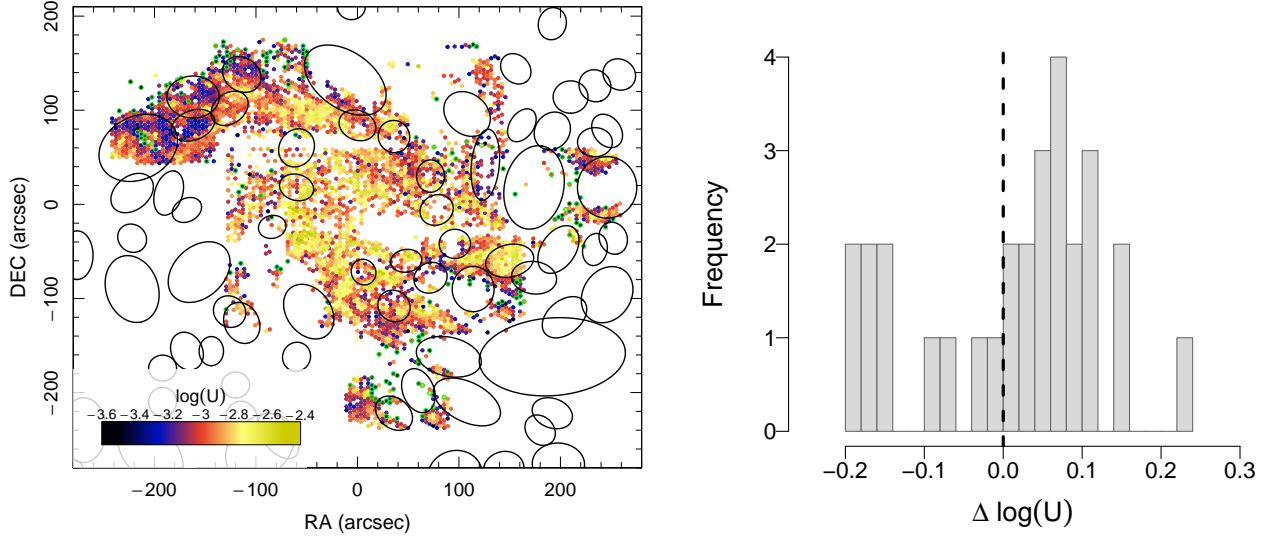
Fig. 10. Ionization parameter in NGC 6946. Left: H I holes (black solid ellipses) superimposed on the log(U) map of NGC 6946. The small green circles indicate DIG dominated fibers. Right: Histogram of the differences $\Delta \log(U) = \widehat{\log(U)}_{rim} - \widehat{\log(U)}_{hole}$, see text for details.

the expanding ejecta, partially destroying the newly formed dust, Bianchi & Schneider 2007; Marassi et al. 2019). The composition and size of grains formed in the SN ejecta that survive the subsequent passage of the reverse shock is still an open question. Recent models suggest that only between 1 to 8% of the observed dust mass produced by SNe will survive and contribute to the ISM (e.g., Bocchio et al. 2016; Sarangi et al. 2018). Taking into account the cumulative effect of the high number of SNR in NGC 6946, it is not surprising we observe a higher dust extinction in the rims of the holes.

On the other hand, the ionization parameter in the rims of the holes shows only a small difference with respect to the holes, although ~66% of the rim's show higher values. The ionization parameter directly reflects the ratio of radiation to gas pressure, or the interaction between the ionizing source and ionizing gas. Therefore, the ionization parameter increases with the luminosity of the stellar population and the hardness of the ionizing radiation field.

It has also been suggested that high ionization parameters are the result of high SFRs, which lead to a larger reservoir of ionizing photons (e.g., Hainline et al. 2009; Kewley et al. 2013). This would be in agreement with the observed enhancement in SFR in the rims of the holes. Hence, the observed difference is likely a result of the enhanced SFR taking place. Another possible effect that could be at play is the dust absorption. On galactic scales, Yeh & Matzner (2012) have suggested that the ionization parameter can be suppressed by selective dust absorption of ionizing photons in the regions where U is highest, decreasing the observed ionization parameter. This suggests that the ionization parameter we observe could be higher.

Finally, we observe only a minor increase in the oxygen abundance in the rims of the holes. Considering that the chemical enrichment produced by the SNe will be mixed into an already enriched ISM (12+log(O/H) ~ 8.5, see Fig. 4), the cumulative effect of the SNe on the ISM metallicity is expected to be small and within the errors.

6. Conclusions

In this paper, we analyze the spiral galaxy NGC 6946, also known as the Fireworks galaxy due to its extremely high num-

ber of SNRs. We link the high number of SNRs with H I holes in NGC 6946, and analyze their optical properties such as the oxygen abundance, SFR surface density, ionization parameter, and the BPT classification. This work relies on the combination of the SNR candidates of Long et al. (2019), the H I holes catalog of Boomsma et al. (2008), and the GMS IFU spectroscopy of Metal-THINGS for NGC 6946. Our findings can be summarized as follows.

– The oxygen abundance of fibers hosting SNRs are in agreement with the rest of our data and follow the general tendency of the metallicity gradient of fibers not hosting SNRs. Altogether, this suggests that SNRs do not contribute significantly to the radiation of the fibers.

– Our data indicate an overabundance of SNRs located around the rims of the H I holes (Fig. 6). This is in agreement with the lack of bright emission at multiple wavelengths inside the holes, suggesting that the H I holes are already devoid of gas, which also could explain the lack of SNRs located inside the holes.

– The overabundance of SNRs in the H I hole rims indicates an enhanced star formation in the very recent past in those regions. Indeed, our IFU data shows a higher star formation rate on the rims compared to within the H I holes (see Fig. 7). This is connected with the overabundance of SNRs, in the sense that expanding shells would compress the surrounding gas and trigger the formation of a new generation of stars. Supporting this effect, our data indicates that the dust extinction is also higher in the rims. Indeed, this result is expected since dust grains increase the molecular formation and enhance the SFR.

– Our analysis provides a hint of an enhanced ionization parameter in the rims for 66% of the analyzed holes, although this is not statistically significant according to the paired t-test (p-value of 0.48). Additionally, our analysis shows only a marginal chemical enrichment, with ~58.6% of holes showing a higher oxygen abundance in the rims. Altogether, our data supports a picture in which multiple SN explosions occurred dozens of Myrs ago, producing the H I holes and compressing the gas and inducing star formation in the rims of the H I holes.

References

Amarsi, A. M., Barklem, P. S., Asplund, M., Collet, R., & Zatsarinny, O. 2018, A&A, 616, A89

Anand, G. S., Rizzi, L., & Tully, R. B. 2018, AJ, 156, 105

Asano, R. S., Takeuchi, T. T., Hirashita, H., & Inoue, A. K. 2013, EP&S, 65, 213

Asari, N. V., Cid, Fernandes R., Stasińska, G., et al. 2007, MNRAS, 381, 263

Bagetakos, I., Brinks, E., Walter, F., et al. 2011, AJ, 141, 23

Baldwin, J. A., Phillips, M. M., & Terlevich, R. 1981, PASP, 93, 5

Belfiore, F., Maiolino, R., Tremonti, C., et al. 2017, MNRAS, 469, 151

Bertin, G., & Amorisco, N. G. 2010, A&A, 512, A17

Bianchi, S., & Schneider, R. 2007, MNRAS, 378, 973

Blais-Ouellette, S., Amram, P., Carignan, C., & Swaters, R. 2004, A&A, 420, 147

Blanc, G. A., Heiderman, A., Gebhardt, K., Evans, N. J., & Adams, J. 2009, ApJ, 704, 842

Bocchio, M., Marassi, S., Schneider, R., et al. 2016, A&A, 587, A157

Bonnarel, F., Boulesteix, J., Georgelin, Y. P., et al. 1988, A&A, 189, 59

Boomsma, R. 2007, Ph.D. Thesis, Groningen, The Netherlands

Boomsma, R., Oosterloo, T. A., Fraternali, F., van der Hulst, J. M., & Sanchisi, R. 2008, A&A, 490, 555

Brinks, E., & Bajaja, E. 1986, A&A, 169, 14

Bruursema, J., Meixner, M., Long, K. S., & Otsuka, M. 2014, AJ, 148, 41

Bruzual, G., & Charlot, S. 2003, MNRAS, 344, 1000

Bundy, K., Bershady, M. A., Law, D. R., et al. 2015, ApJ, 798, 7

Cairós, L. M., Caon, N., García-Lorenzo, B., et al. 2012, A&A, 547, A24

Calzetti, D. 2013, Secular Evolution of Galaxies, eds. J. Falcón-Barroso, & J. H. Knapen (Cambridge, UK: Cambridge University Press), 419

Calzetti, D., Kinney, A. L., & Storchi-Bergmann, T. 1994, ApJ, 429, 582

Calzetti, D., Kinney, A. L., & Storchi-Bergmann, T. 1996, ApJ, 458, 132

Calzetti, D., Armus, L., Bohlin, R. C., et al. 2000, ApJ, 533, 682

Cardelli, J. A., Clayton, G. C., & Mathis, J. S. 1989, ApJ, 345, 245

Carignan, C., Charbonneau, P., Boulanger, F., & Viallefond, F. 1990, A&A, 234, 43

Cid Fernandes, R., Mateus, A., Sodré, L., Stasińska, G., & Gomes, J. M. 2005, MNRAS, 358, 363

Cid Fernandes, R., Stasińska, G., Schlickmann, M. S., et al. 2010, MNRAS, 403, 1036

Collins, J. A., Benjamin, R. A., & Rand, R. J. 2002, ApJ, 578, 98

Daigle, D., Carignan, C., Amram, P., et al. 2006, MNRAS, 367, 469

de Blok, W. G. G., Walter, F., Brinks, E., et al. 2008, AJ, 136, 2648

de Vaucouleurs, G., de Vaucouleurs, A., Corwin, H. G., et al. 1991, Third Reference Catalog of Bright Galaxies (New York: Springer Verlag)

Dors, O. L., Hägele, G. F., Cardaci, M. V., & Krabbe, A. C. 2017, MNRAS, 466, 726

Dib, S., & Burkert, A. 2005, ApJ, 630, 238

Dib, S., Bell, E., & Burkert, A. 2006, ApJ, 638, 797

Dib, S., Braine, J., Gopinathan, M., et al. 2021, A&A, 655, A101

Eldridge, J. J., & Xiao, L. 2019, MNRAS, 485, L58

Elmegreen, D. M., Chromey, F. R., & Santos, M. 1998, AJ, 116, 1221

Fathi, K., Beckman, J. E., Piñol-Ferrer, N., et al. 2009, ApJ, 704, 1657

Hainline, K. N., Shapley, A. E., Kornei, K. A., et al. 2009, ApJ, 701, 52

Helfer, T. T., Thornley, M. D., Regan, M. W., et al. 2003, ApJS, 145, 259

Hill, G. J., MacQueen, P. J., Smith, M. P., et al. 2008, SPIE Conf. Ser., 7014

Hollenbach, D., & McKee, C. F. 1979, ApJS, 41, 555

Jarrett, T. H., Cluver, M. E., Brown, M. J. I., et al. 2019, ApJSS, 245, 25

Kaplan, K. F., Jogee, S., Kewley, L., et al. 2016, MNRAS, 462, 1642

Kauffmann, G., Heckman, T. M., Tremonti, C., et al. 2003, MNRAS, 346, 1055

Kennicutt, R. C., Hao, C.-N., Calzetti, D., et al. 2009, ApJ, 703, 1672

Kennicutt, R. C., Calzetti, D., Aniano, G., et al. 2011, PASP, 123, 1347

Kewley, L. J., Dopita, M. A., Sutherland, R. S., Heisler, C. A., & Trevena, J. 2001, ApJ, 556, 121

Kewley, L. J., Dopita, M. A., Leitherer, C., et al. 2013, ApJ, 774, 100

Kopsacheili, M., Zezas, A., & Leonidaki, I. 2020, MNRAS, 491, 889

Kormendy, J., Drory, N., Bender, R., & Cornell, M. E. 2010, ApJ, 723, 54

Kreckel, K., Ho, I.-T., Blanc, G. A., et al. 2019, ApJ, 887, 80

Kroupa, P. 2001, MNRAS, 322, 231

Lacey, C. K., & Duric, N. 2001, ApJ, 560, 719

Lacey, C. K., Duric, N., & Goss, W. M. 1997, ApJSS, 109, 417

Lara-López, M. A., Hopkins, A. M., López-Sánchez, A. R., et al. 2013, MNRAS, 434, 451

Lara-López, M. A., Zinchenko, I. A., Pilyugin, L. S., et al. 2021, ApJ, 906, 42

Lara-López, M. A., Galán-de Anta, P. M., Sarzi, M., et al. 2022, A&A, 660, A105

Larsen, S. S. 2004, A&A, 416, 537

Lee, H., Skillman, E. D., & Venn, K. A. 2005, ApJ, 620, 223

Leroy, A. K., Walter, F., Bigiel, F., et al. 2009, AJ, 137, 4670

Long, K. S., Winkler, P. F., & Blair, W. P. 2019, ApJ, 875, 85

Long, K. S., Blair, W. P., Winkler, P. F., & Lacey, C. K. 2020, ApJ, 899, 14

Marassi, S., Schneider, R., Limongi, M., et al. 2019, MNRAS, 484, 2587

Mateus, A., Sodré, L., Cid, Fernandes R., et al. 2006, MNRAS, 370, 721

Mathewson, D. S., & Clarke, J. N. 1973, ApJ, 180, 725

Matonick, D. M., & Fesen, R. A. 1997, ApJS, 112, 49

Mo, H. J., Mao, S., & White, S. D. M. 1998, MNRAS, 295, 319

Mogitsi, K. M., de Blok, W. J. G., Caldú-primo, A., et al. 2016, AJ, 151, 15

Moustakas, J., Kennicutt, R. C., Tremonti, C. A., et al. 2010, ApJS, 190, 233

Murphy, J. W., Khan, R., Williams, B., et al. 2018, ApJ, 860, 117

Osterbrock, D. E. 1989, Astrophysics of Gaseous Nebulae and Active Galactic Nuclei (Mill Valley, CA: University science books)

Poetrodjojo, H., D'Agostino, J. J., Groves, B., et al. 2019, MNRAS, 487, 79

Pilyugin, L. S., & Grebel, E. K. 2016, MNRAS, 457, 3678

Pilyugin, L. S., Vílchez, J. M., & Contini, T. 2004, A&A, 425, 849

Pilyugin, L. S., Lara-López, M. A., Grebel, E. K., et al. 2013, MNRAS, 432, 1217

Pilyugin, L. S., Grebel, E. K., & Kniazev, A. Y. 2014, AJ, 147, 131

Pilyugin, L. S., Grebel, E. K., Zinchenko, I. A., et al. 2018, A&A, 613, A1

Pilyugin, L. S., Grebel, E. K., Zinchenko, I. A., Nefedyev, Y. A., & Vílchez, J. M. 2019, A&A, 623, A122

Pilyugin, L. S., Grebel, E. K., Zinchenko, I. A., et al. 2020a, A&A, 634, A26

Pilyugin, L. S., Grebel, E. K., Zinchenko, I. A., et al. 2020b, A&A, 639, A96

Pilyugin, L. S., Cedrés, B., Zinchenko, I. A., et al. 2021a, A&A, 653, A11

Pilyugin, L. S., Zinchenko, I. A., Lara-López, M. A., Nefedyev, Y. A., & Vílchez, J. M. 2021b, A&A, 646, A54

Points, A. E., Long, K. S., Winkler, P. F., & Blair, W. P. 2019, ApJ, 887, 66

Reynolds, R. J. 1984, ApJ, 282, 191

Rogstad, D. H., & Shostak, G. S. 1972, ApJ, 176, 315

Romeo, A. B., & Fathi, K. 2015, MNRAS, 451, 3107

Sarangi, A., Matsuura, M., & Micelotta, E. R. 2018, SSRv, 214, 63

Schinnerer, E., Böker, T., Emsellem, E., & Lisenfeld, U. 2006, ApJ, 649, 181

Sharina, M. E., Karachentsev, I. D., & Tikhonov, N. A. 1997, Astron. Lett., 23, 273

Storey, P. J., & Zeippen, C. J. 2000, MNRAS, 312, 813

Tody, D. 1986, SPIE Conf. Ser., 627, 733

Trachternach, C., de Blok, W. G. G., Walter, F., Brinks, E., & Kennicutt, R. C. 2008, AJ, 136, 2720

Walsh, W., Beck, R., Thuma, G., et al. 2002, A&A, 388, 7

Walter, F., Brinks, E., de Blok, W. J. C., et al. 2008, AJ, 136, 2563

White, S. D. M., & Frenk, C. S. 1991, ApJ, 379, 52

Yeh, S. C. C., & Matzner, C. D. 2012, ApJ, 757, 108

Zaritsky, D., Kennicutt, R. C., & Huchra, J. P. 1994, ApJ, 420, 87

Zinchenko, I. A., Pilyugin, L. S., Grebel, E. K., Sánchez, S. F., & Vílchez, J. M. 2016, MNRAS, 462, 2715

Zinchenko, I. A., Pilyugin, L. S., Sakhibov, F., et al. 2019, A&A, 628, A55

Zinchenko, I. A., Vílchez, J. M., Pérez-Montero, E., et al. 2021, A&A, 655, A58